



Accuracy improvement of demodulating the stress field with StressUnet in photoelasticity

WEILIANG ZHAO, GUANGLEI ZHANG, ^{ID} AND JIEBO LI^{*} ^{ID}*Institute of Medical Photonics, Beijing Advanced Innovation Center for Biomedical Engineering, School of Biological Science and Medical Engineering, Beihang University, Beijing 100191, China***Corresponding author: jiebo39@buaa.edu.cn**Received 20 May 2022; revised 8 September 2022; accepted 8 September 2022; posted 9 September 2022; published 3 October 2022*

Evaluating the stress field based on photoelasticity is of vital significance in engineering fields. To achieve the goal of efficiently demodulating stress distribution and to overcome the limitations of conventional methods, it is essential to develop a deep learning method to simplify and accelerate the process of image acquisition and processing. A framework is proposed to enhance prediction accuracy. By adopting Resnet as the backbone, applying U-Net architecture, and adding a physical constraint module, our model recovers the stress field with higher structural similarity. Under different conditions, our model performs robustly despite complicated geometry and a large stress range. The results prove the universality and effectiveness of our model and offer an opportunity for instant stress detection. © 2022 Optica Publishing Group

<https://doi.org/10.1364/AO.464466>

1. INTRODUCTION

Principal stress differences and their orientations can be obtained by photoelasticity basically based on the phenomenon of stress-induced birefringence [1]. Due to the merits of high sensitivity and precision, non-contact aspect [2], simplicity, and low cost, photoelasticity has been widely used for stress measurement in engineering fields such as glass [3], electronic devices [4], and optical elements [5] to guarantee the quality of products since their residual stress strongly affects their performance. With the rapid development of digital photoelasticity [6], digital images containing whole field stress information are recorded and processed for quantitative evaluation. That requires a large computational amount, bringing difficulty to instant stress evaluation. Therefore, an efficient image processing algorithm based on photoelasticity is of vital significance to real-time stress evaluation.

Currently, many traditional photoelasticity techniques have been proposed to measure stress, including the carrier fringe method [7], phase-shifting techniques [8], and twelve fringe photoelasticity (TFP) [9]. Among these methods, by introducing the carrier into the light path, the carrier fringe method successfully obtains the composite fringe, whose retardation is the superposition of the carrier and sample. However, its application is limited to the condition that the residual retardation is constant in the direction perpendicular to the carrier fringes. Another more mature approach, the phase-shifting method, is a technique that uses different phase images containing modulation information to resolve the retardation by rotating optical elements. Taking more images is on one hand capable of reducing the wave plate mismatch error and algorithm sensitivity, but

on the other hand much more time consuming. By contrast, TFP tackles fringe order estimation by capturing a single image and comparing points with a calibration image. Nevertheless, it has a limitation that the resolvable fringe order is up to 12, and acquiring experimental calibration images instead of theoretically generating a calibration table is laborious. Similarly, a novel method that combined white light photoelasticity and spectrometry achieved low-level stress measurement [10], but needed to establish a database beforehand. Conventional data acquisition and processing have limitations that cannot meet the needs of instant detection, thus inspiring us to search for more effective algorithms.

Since deep learning was introduced into computer vision, it has achieved remarkable results in various tasks such as image classification [11], object detection [12], and image segmentation [13], and surpassed analytic methods in solving substantial inverse problems in imaging [14]. Its universality and effectiveness inspired us to apply it to photoelasticity image processing, specifically, predicting stress distribution through digital photoelasticity. Among deep learning frameworks, the convolutional neural network achieved remarkable performance due to its capability of capturing and extracting spatial features. Briñez de León proposed PhotoelastNet, a fully convolutional network that performed an averaged 92.41% score according to the structural similarity (SSIM) metric [15]. However, it does not make full use of global fringe information, and the model is still not sufficiently robust. A similar and more complete work was presented in [16]. By increasing the channels and adding batch normalizations, the proposed stress recovery network could achieve higher performance. Nonetheless, more parameters

need more storage and may bring longer computational time. Therefore, we endeavored to enhance prediction accuracy and robustness without adding parameters.

In this work, we propose a new framework named StressUnet, designed for deducing stress evaluation from a digital photoelasticity image. Compared with the traditional U-Net, we added a physical constraint module to make full use of physical information and make the framework more suitable for handling the physical task. To ensure the universality of the network, we used a dataset containing a variety of scenarios for training. The experimental results proved the effectiveness of our proposed network, and it is expected to be applied in instant stress evaluation.

2. METHOD

A. Isochromatic Images

In the plane stress model, a microbody is subjected to normal stresses σ_x and σ_y and shear stress $\tau_x = \tau_y$, as shown in Fig. 1(a). According to the stress circle, at a particular section parallel to the z axis, the maximum and minimum normal stresses are calculated as

$$\left. \begin{array}{l} \sigma_{\max} \\ \sigma_{\min} \end{array} \right\} = \frac{\sigma_x + \sigma_y}{2} \pm \sqrt{\left(\frac{\sigma_x - \sigma_y}{2} \right)^2 + \tau_x^2}. \quad (1)$$

The azimuth angle α_0 of the section where the maximum normal stress σ_{\max} exists can be determined by Eq. (2):

$$\tan 2\alpha_0 = \frac{2\tau_x}{\sigma_x - \sigma_y}, \quad (2)$$

where σ_{\max} and σ_{\min} are also called the first principal stress σ_1 and second principal stress σ_2 , respectively, and α_0 denotes the principal stress azimuth as shown in Fig. 1(b).

Birefringence occurs when light travels through the $x - y$ plane of a microbody perpendicularly. According to the stress-optic law, the difference in the refractive index between the two beams is proportional to the difference between σ_1 and σ_2 :

$$n_1 - n_2 = C(\sigma_1 - \sigma_2). \quad (3)$$

Hence, the phase delay δ of the two beams is proportional to the difference between σ_1 and σ_2 :

$$\delta = \frac{2\pi dC(\sigma_1 - \sigma_2)}{\lambda}, \quad (4)$$

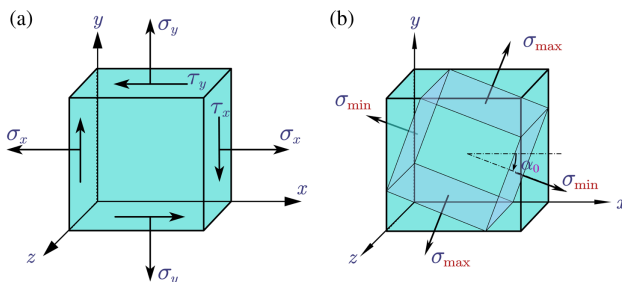


Fig. 1. Illustration of plane stress model. (a) General form of plane stress state. (b) Maximum and minimum stress of plane stress state.

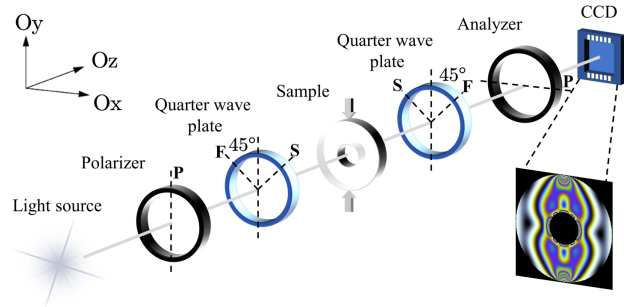


Fig. 2. Schematic diagram of isochromatic image acquisition by an orthogonal circular polarization field configuration.

where C represents the stress optical coefficient of the material, d is the thickness of the light passing through the object, and λ refers to the wavelength of light.

A classical polarization field that can obtain photoelasticity images is the orthogonal plane polarization field (dark field), as shown in Fig. 2. When white light passes through a polarizer, quarter-wave plate, sample, quarter-wave plate, and analyzer in turn to reach the CCD, we can obtain the isochromatic image of the sample.

The intensity of the stress model in an orthogonal circularly polarized optical system can be expressed as

$$I = \frac{1}{\lambda_2 - \lambda_1} \int_{\lambda_1}^{\lambda_2} I_a(\lambda) \sin^2 \left(\frac{\pi \Delta c_\lambda}{\lambda} \frac{c_\lambda}{c_0} \right) \left(1 - \cos^2 2\alpha_0 \sin^2 \xi \right) d\lambda, \quad (5)$$

where λ_2 and λ_1 denote the maximum and minimum wavelength of the light source spectrum, respectively, $\frac{c_\lambda}{c_0}$ denotes scattering in birefringence, and ξ represents the mismatch error brought by the quarter-wave plate.

When white light passes through birefringent materials with stress, different stresses at each point cause different phase delays, so interference enhancement or interference attenuation may occur. As C is a function of λ , interference enhancement presents at different wavelengths. We can regard it as a forward process that visualizes the photoelasticity image as output with the stress distribution as input, while demodulating the stress map with the photoelasticity image as input can be considered an inverse problem [15]. Unfortunately, the relationship between stress and light intensity in the inverse process is difficult to formulate explicitly.

Researchers established TFP [9] based on a one-to-one correspondence between RGB values and fringe levels, but the method had the limitation that it can be applied only in a finite stress range, as this correspondence no longer holds in a large stress range. It implies that light intensity information and spatial information need to be considered conjunctively to resolve the stress distribution. Based on this, we further explored the physical constraint and contrived a new model, called StressUnet, which will be fully demonstrated in the following section.

B. Network Architecture

The overall architecture of our proposed StressUnet is shown in Fig. 3. It consists mainly of three modules: encoder, decoder, and

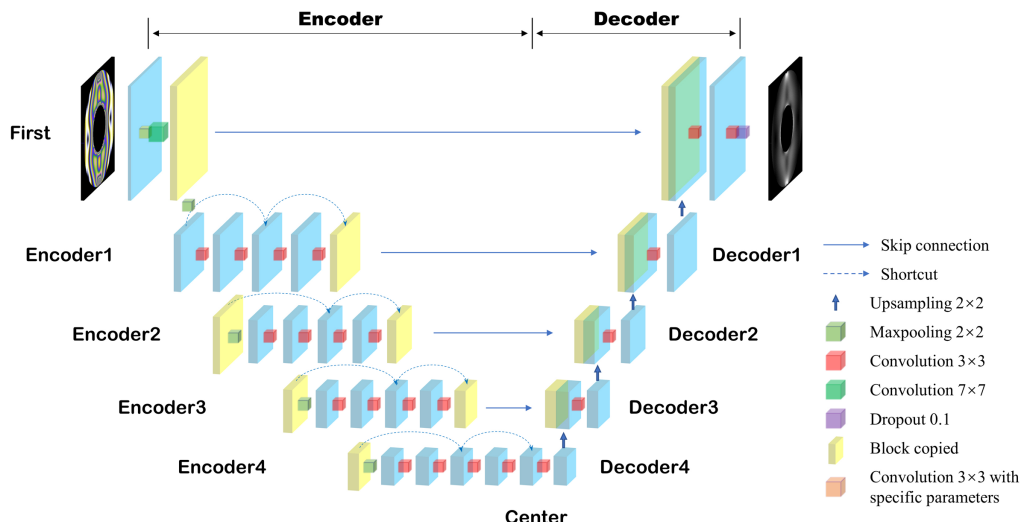


Fig. 3. Schematic of StressUnet. All convolution operations used appropriate padding to retain the shape of the blue block.

constraint. Given an isochromatic image, it first goes through the encoder to extract hierarchical stress features, then the decoder aggregates multi-scale features to generate the preliminary stress distribution, which is finally refined by the constraint module and output prediction.

The encoder and decoder constitute the U-Net structure. U-Net was originally applied in the field of medical image segmentation [17]. Inspired by the fringe grading method [18], the global fringe characteristic is of vital significance to demodulate the isochromatic image.

Deducing by using a Jones vector and Jones matrix, the output intensity of the orthogonal plane polarization field is

$$I_{\perp} = I_a \sin^2 2\theta \sin^2 \frac{\delta}{2}, \quad (6)$$

where I_a is the amplitude of incoming light intensity, θ represents the principal stress direction, and δ denotes the phase delay. When interference attenuation occurs, $\sin^2 \frac{\delta}{2} = 0$, that is, $\delta = 2N\pi$, $N = 0, 1, 2, \dots$. Substituting this into the stress-optic law, we can obtain

$$N = \frac{h(\sigma_1 - \sigma_2)}{f_{\sigma}}, \quad (7)$$

where f_{σ} denotes the material fringe value.

Therefore, we can determine the stress according to its fringe order. Fringe grading requires global information, while fine stress distribution needs local information. In the process of convolution and downsampling, local information will inevitably be lost if using fully convolutional network architecture. To compensate for the loss of local information, U-Net adds skip connections [17]. It is beneficial for our task to integrate global fringe features and local color features, so we adopted U-Net architecture.

The backbone of our encoder is Resnet [19], which has been widely used, proving its effectiveness and stability. For deep neural networks, adding short connections can prevent overfitting and enhance generalization ability. Considering the image size

Table 1. Encoder and Decoder Parameters of Each Block^a

Block	Input Size	Output Size
First block	224 * 224 * 3	112 * 112 * 64
Encoder1	112 * 112 * 64	56 * 56 * 64
Encoder2	56 * 56 * 64	28 * 28 * 128
Encoder3	28 * 28 * 128	14 * 14 * 256
Encoder4	14 * 14 * 256	7 * 7 * 512
Center	7 * 7 * 512	14 * 14 * 512
Decoder4	14 * 14 * 512	28 * 28 * 256
Decoder3	56 * 56 * 128	112 * 112 * 64
Decoder2	112 * 112 * 64	224 * 224 * 64
Decoder1	224 * 224 * 64	224 * 224 * 1

^aThe first two numbers of the size indicate the size of the image, and the last number indicates the channels of the image.

of the dataset, Resnet18 is sufficient for capturing fringe details. Specific parameters are shown in Table 1.

Benefiting from the sufficiently large receptive field of the encoder, our decoder is designed to be lightweight and efficient. Unifying hierarchical fringe features from the encoder by unsampling and concatenating, local information about stress variation and global information about fringe order are synthesized to speculate an elementary stress distribution.

On the basis of U-Net and Resnet, we also added the physical constraint module. The plane stress model satisfies the Laplace equation of difference

$$D_s = \frac{bcd}{(ab+cd)(a+b)} D_a + \frac{acd}{(ab+cd)(a+b)} D_b \\ + \frac{abd}{(ab+cd)(a+b)} D_c + \frac{abc}{(ab+cd)(a+b)} D_d, \quad (8)$$

where D means the sum of principal stress, D_a , D_b , D_c , D_d denote D values of the adjacent four points around point S , and a, b, c, d are the distances between S and adjacent points. In an image, the distance between a pixel and the adjacent four points is equal, so Eq. (8) can be simplified as

$$D_s = \frac{(D_a + D_b + D_c + D_d)}{4}. \quad (9)$$

Consequently, the stress value of point S in the output stress field prediction should be the average of the stress values of the adjacent four points, and correspondingly, the average of the gray value in the image. Inspired by the theory, the constraint module is added to adjust the stress distribution to make it be consistent with the physical constraint. Specifically, we added five convolution layers between the preliminary stress distribution and the output image. The convolution kernel of each layer is $3 * 3$ size, with constant parameters c :

$$c = \begin{pmatrix} 0 & 0.25 & 0 \\ 0.25 & 0 & 0.25 \\ 0 & 0.25 & 0 \end{pmatrix}. \quad (10)$$

Instead of adding physical loss into the loss function, it avoided introducing more hyper-parameters, meanwhile retaining the same number of parameters of the whole framework, as the parameters in the constraint are constant.

C. Photoelasticity Dataset

Presently, training a deep neural network to achieve remarkable performance requires a large quantity of images that are laborious to record; thus, computational images are generated and utilized. We trained and tested our model based on a public dataset [20]. This dataset provides photoelasticity images and corresponding stress distribution images. Several factors are taken into account, including light source, camera sensors, stressed sample geometry, and stress magnitude. In terms of the light source, constant in the visible range, incandescent, fluorescent, white LED, and a cold white laser are selected, which are commonly used in the literature. In the case of camera sensors, human vision response, Sony IMX250, and DCU3260 are selected. Besides conventional stress models such as compressed disk, ring and plate, ring under rotation, and bending are further considered. In contrast to traditional photoelasticity cases, images from other research fields are added into the dataset, including saliency maps, Gaussian distributions, and 3D reconstruction. In these images, some regions contain more irregular and denser fringes, which indicate more dramatic stress variation, and hence, it is hard to resolve the stress distribution. With respect to stress magnitude, max stress magnitude of each case varies from 12 to 72 MPa and is a multiple of 12 MPa. For analytical stress maps, the material is assumed to be PMMA material with 10 mm thickness and a $4.5 * 10^{-12}$ stress optic coefficient.

Due to the insufficiency of photoelasticity cases, data augmentation was applied. The main measures are cropping or rotating original images if practicable. For cropping operation, four regions of each image are chosen and four images are derived. For rotation, 90° , 180° , and 270° rotations are executed, and thus three extra images are obtained. In total, the dataset contains 101,430 photoelasticity images and their respective stress maps.

D. Loss Function and Evaluation Metrics

The loss function is the weighted sum of SSIM [21] and mean square error (MSE). Given a reference image r and a predicted

image p , both of size $m \times n$, the SSIM between r and p is defined by

$$\text{SSIM}(r, p) = \frac{(2\mu_r\mu_p + C_1)(2\sigma_{rp} + C_2)}{(\mu_r^2 + \mu_p^2 + C_1)(\sigma_r^2 + \sigma_p^2 + C_2)}, \quad (11)$$

where μ_r , σ_{rp} , and σ_r are specifically calculated by

$$\mu_r = \frac{1}{N} \sum_{i=1}^N r_i, \quad (12)$$

$$\sigma_{rp} = \frac{1}{N-1} \sum_{i=1}^N (r_i - \mu_r)(p_i - \mu_p), \quad (13)$$

$$\sigma_r = \left(\frac{1}{N-1} \sum_{i=1}^N (r_i - \mu_r)^2 \right)^{\frac{1}{2}}. \quad (14)$$

MSE is defined as

$$\text{MSE}(r, p) = \frac{1}{mn} \sum_{i=1}^m \sum_{j=1}^n (r_{ij} - p_{ij})^2. \quad (15)$$

SSIM is proposed to solve the problem that MSE is disturbed greatly by specific values and does not conform to the visual perception of the human visual system to pictures [21]. In the training process, we found that using SSIM as the loss function reduced the noise in stress maps. The stress maps were smoother compared with the stress maps predicted by the trained model using MSE as the loss function. Since the appearance of noise indicates a significant change of stress, which contradicts the Laplace equation, we believe that SSIM is beneficial for the neural network to learn the stress variation. Nevertheless, MSE is sensitive to the area with high stress, which is beneficial to predict the maximum stress. MSE is crucial in the industry for preventing damage or failure caused by stress, so it is essential that MSE be accounted for in the loss function. Therefore, we used the combination of SSIM and MSE as our loss function. Specifically, loss function L is set as follows:

$$\mathcal{L}(\Theta) = 1 - \text{SSIM}(r, p) + \lambda \text{MSE}(r, p), \quad (16)$$

where λ adopts a segmented strategy.

At the beginning of the training, the loss function was the sum of SSIM and MSE. After 50 epochs, since our network had learned rough stress distribution, we appropriately increased the weight of MSE to make the network pay more attention to the zones with high stress. The setting of λ is as follows:

$$\lambda = \begin{cases} 1, & \text{epoch} \leqslant 50 \\ 1 + 0.2(\text{epoch} - 50) & \text{epoch} > 50 \end{cases}. \quad (17)$$

We selected three metrics to evaluate the quality of recovered stress distribution: SSIM, MSE, and peak signal to noise ratio (PSNR). Besides SSIM and MSE, PSNR is also an authoritative image quality evaluation metric [22]. Given a reference image r and a predicted image p , the PSNR between r and p is calculated as

$$\text{PSNR}(r, p) = 10 \log_{10} \left(\frac{255^2}{\text{MSE}(r, p)} \right), \quad (18)$$

where MSE has the same definition as Eq. (15).

According to the definitions of Eqs. (11), (15), and (18), the higher SSIM is, closer to one, means the more similar the predicted stress map is to the ground truth stress map; a higher PSNR means better prediction, while a lower MSE means the smaller the prediction error and the better the predicted result.

E. Training and Testing

Considering the training time and the performance of the model, we set three training groups, where 1000, 5000, and 10,000 images were selected equidistantly from the original dataset as the training set. This strategy guaranteed the model learning characteristics of various types of light sources and camera sensors, and enhanced the generalization ability. The validation set used in the training involved 2000 images selected equidistantly in the original dataset. For every epoch, we trained our model on the training set, and then tested its performance on the validation set and saved the model parameters if its result on SSIM surpassed the previous best result. For the test set, 10,000 images were selected equidistantly to make them statistically significant.

For other settings, the Adam optimizer was chosen as our network optimizer [23]. We trained the model for 60 epochs, and the learning rate was set to be 1e-4 at the first 50 epochs and 1e-5 at the last 10 epochs, with a batch size of 128. All training and testing were implemented in Pytorch [24] on a desktop with AMD 16-Core Processor to 3.40 GHz, 47.9 Gb RAM. The code is available in Ref. [25].

3. RESULTS

A. Evaluation on Test Set

To verify the prediction accuracy and universality of our proposed framework, we tested our model on a large dataset. Referring to PhotoelastNet proposed by Bríñez de León [15], we compared our results with its results on SSIM, PSNR, and MSE, as shown in Table 2. On the whole dataset, our model achieved 0.979 on SSIM, greatly surpassing PhotoelastNet achieving 0.92. On completing the 0.05 improvement, we used a training set containing only 10,000 images, an amount that was 93.8% less than the control group. Training epochs decreased from 100 to 60, reducing 40%. Fewer training images and less training time proved that our model is capable of effectively capturing the global relationship between intensity and stress and utilizing the fringe information in images. In terms of PSNR, we achieved comparable performance with PhotoelastNet.

Table 2. Quantitative Evaluation Results on Test Set^a

Training Images	Training Epoch	Model	SSIM	PSNR
162,288	100	PhotoelastNet	0.9241	37.2813
10,000	60	StressUnet (with constraint)	0.9790	36.0953
10,000	60	StressUnet (without constraint)	0.9789	35.1607

^aBold numbers denote the highest scores. SSIM and PSNR are evaluated for different methods.

To verify the robustness and universality of our proposed StressUnet, we tested our model from different aspects. As shown in Fig. 4, we considered various geometries of a stressed body under the same conditions of light source, camera sensor, and maximum stress. These cases covered most scenarios, whether global or patched, symmetrical or asymmetrical, compressing or bending, as can usually be seen in validation [4,26]. StressUnet successfully coped with diverse cases even though the geometry of a stressed body was complicated, such as the 3D scanning dragon in the right column. Although it was easier for our model to predict symmetry stress distribution rather than a patch cropped from the global image, the lowest SSIM of all cases was higher than 0.98. It verifies that our model has a general understanding of the stress field and is capable of distinguishing low-stress areas and high-stress areas.

We also evaluated our model from the stress magnitude aspect. Figure 5 is the result of cases when the light source and camera sensor remain the same and there is a gradual increase in stress magnitude. We selected a classical compressed ring as representative [27,28]. Despite the large range of the max stress magnitude, from 12 to 72 MPa, our model behaved robustly. As the stress increased, the performance slightly decreased. However, it was still over 98% according to the SSIM metric. In terms of PSNR and MSE, the worst result surpassed 34 according to PSNR and was smaller than 26 on MSE.

To avoid the destruction brought by excessive stress, the accuracy in the local parts is also crucial, especially for zones with high density fringes. Hence, we evaluated our model on the classical case whose zone was manually defined, as can be seen in Fig. 6.

Compared with the result of the whole image, the performance decreased. However, all results were over 0.95 in SSIM. In terms of PSNR and MSE, the worst result surpassed 25 according to PSNR and was smaller than 200 on MSE. From 48 to 72 MPa, our model behaved stably on three metrics.

If using TFP, light sources and camera sensors would affect prediction accuracy, so a color comparison table was required per every experimental condition [9]. With the same single polariscope configuration condition, we tested our model under different optical parameters to verify whether the performance would be influenced. For the light source, incandescent [29], fluorescent [30], and LED [31] were considered, while for the camera, human vision and Sony CCDs were chosen [32]. Although there was an influence by the configuration combination of light source and camera sensor as shown in Fig. 7, our model was marginally affected, as it was over 94% in all situations according to the SSIM metric. Our model performed better when the light source was LED.

The model was also evaluated when dealing with experimental cases. In our experiment, we used a LED (Daheng GCI-060411) as the light source and a SONY CCD as the camera, then applied a force to a PMMA ring with an outer diameter of 20 mm, inner diameter of 10 mm, and thickness of 10 mm. Isochromatic images were taken in a circularly polarized dark field. The reference was generated by simulation. The test results are shown in Fig. 8. In this case, the SSIM remained over 0.85, proving the availability of our model.

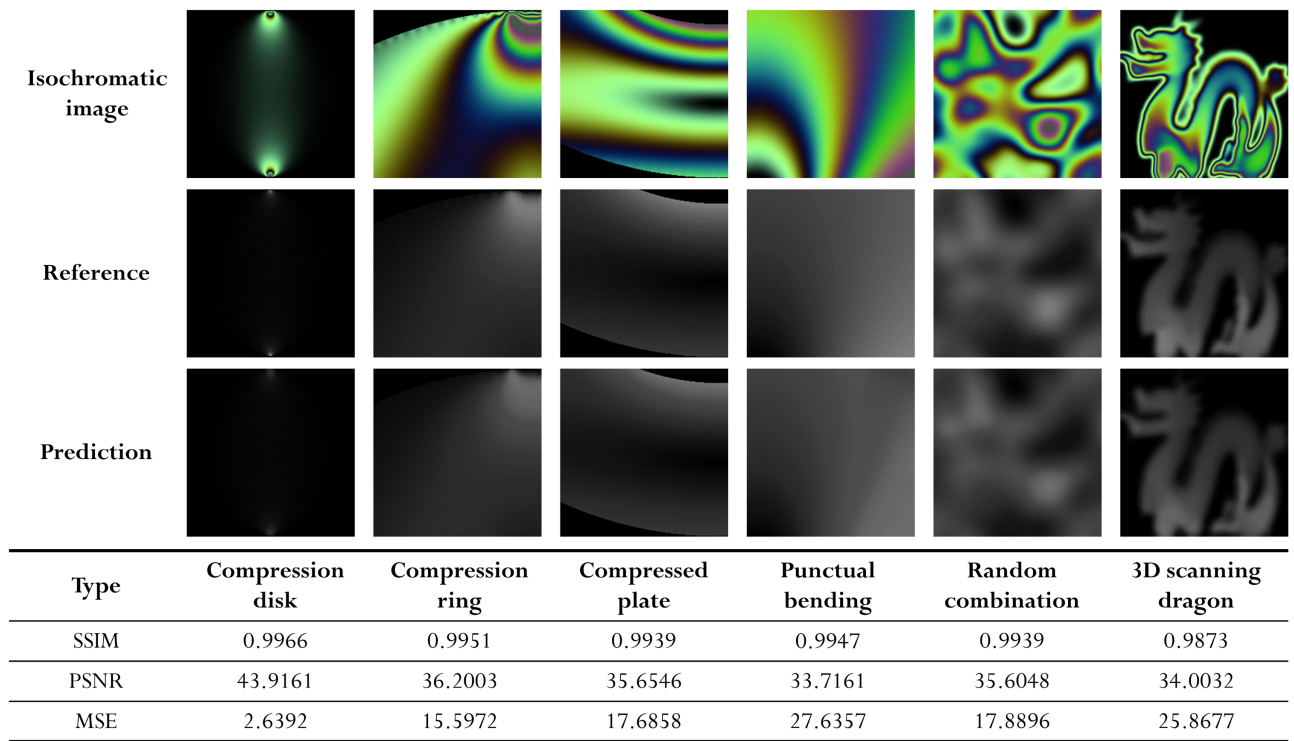


Fig. 4. Predicted stress maps of isochromatic images by using StressUnet and evaluation results on SSIM, PSNR, and MSE. The maximum magnitude of stress in each image is 36 MPa, with a cold white laser as the light source and Sony IMX250 as the camera sensor.

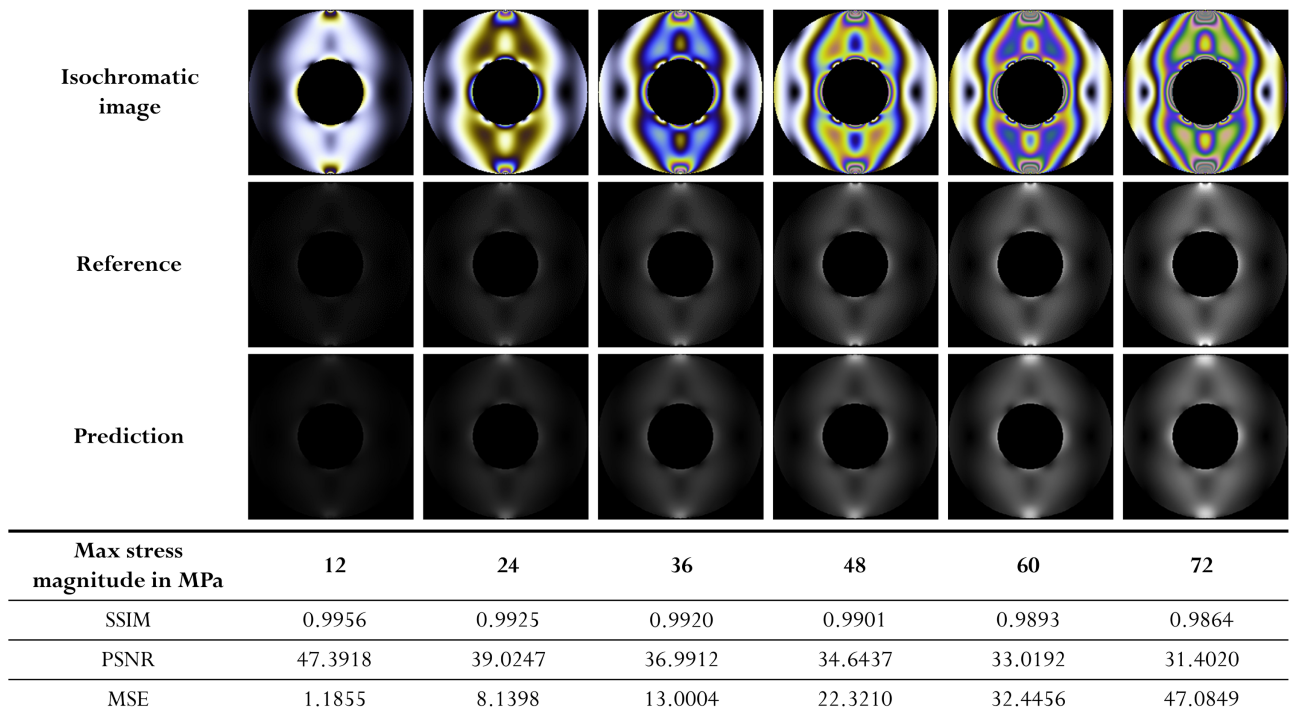


Fig. 5. Predicted stress maps of isochromatic images by using StressUnet and evaluation results on SSIM, PSNR, and MSE. The sample is a compressed ring, with a constant light source and human vision as the camera sensor. The max stress magnitude varies from 12 to 72 MPa and is a multiple of 12 MPa.

B. Effectiveness of the Constraint Module

In this section, we ablate the significant design module in the proposed StressUnet, the constraint module, using different numbers of training sets and testing on the validation set.

As shown in Fig. 9, we presented the changes of the model with or without the constraint module on the validation set according to the SSIM metric during the training process. Regardless of the size of the training set and parameter

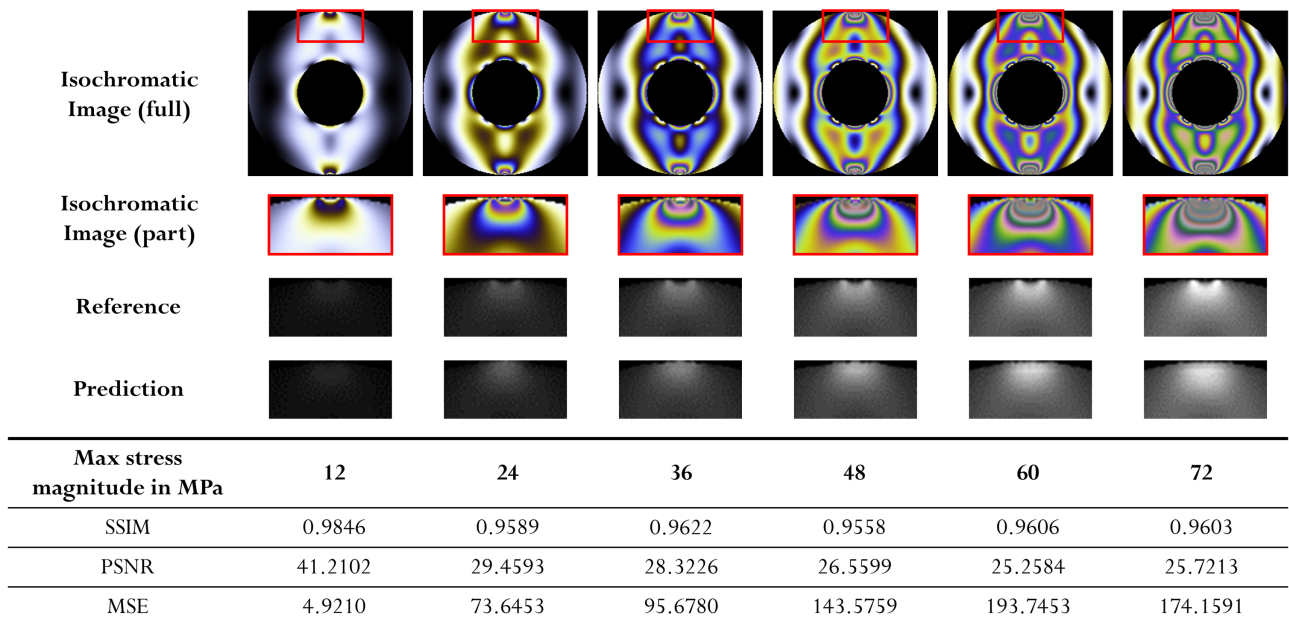


Fig. 6. Predicted local stress maps of isochromatic images' local parts by using StressUnet and evaluation results on SSIM, PSNR, and MSE. The sample is a compressed ring, with a constant light source and human vision as the camera sensor. The max stress magnitude varies from 12 to 72 MPa and is a multiple of 12 MPa.

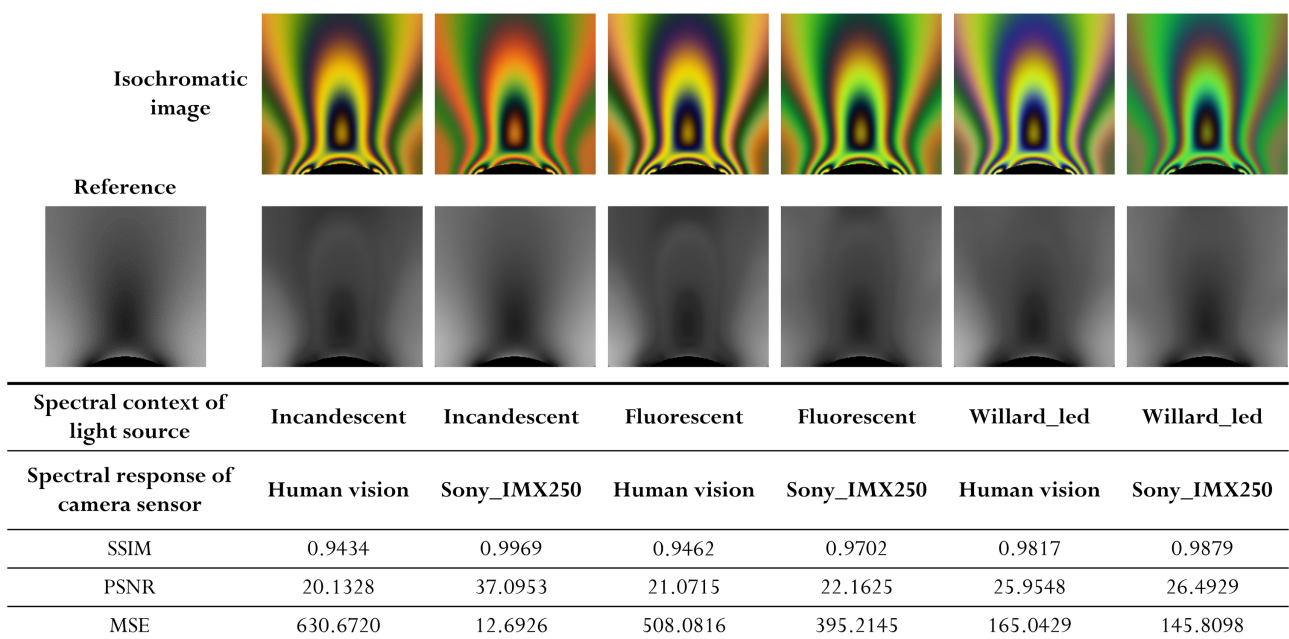


Fig. 7. Predicted stress maps of isochromatic images by using StressUnet and evaluation results on SSIM, PSNR, and MSE. The sample is a ring under punctual bending with maximum stress 48 MPa, analyzed with different light sources and camera sensors.

initialization, StressUnet with the constraint module rapidly converged closely to one and kept stable after 20 epochs, while StressUnet without the constraint module always had dramatic fluctuation. It revealed that the constraint module is capable of regularizing parameters in the neural network to make the prediction reasonable. Moreover, it can be observed from the graph that the model without the constraint module achieved comparable performance after training 40 epochs by using 10,000 images, while the model with the constraint module required

only 10 training epochs with 50% of the training images or the same epochs but 10% of the training images. Therefore, it is less time consuming to well train the network, and there is a strong possibility to obtain the best result by adding the constraint module.

Further comparisons were done using the test set according to SSIM, PSNR, and MSE metrics, presented in Table 3. When the training dataset was relatively small, 1000, StressUnet with the constraint module far exceeded StressUnet without the

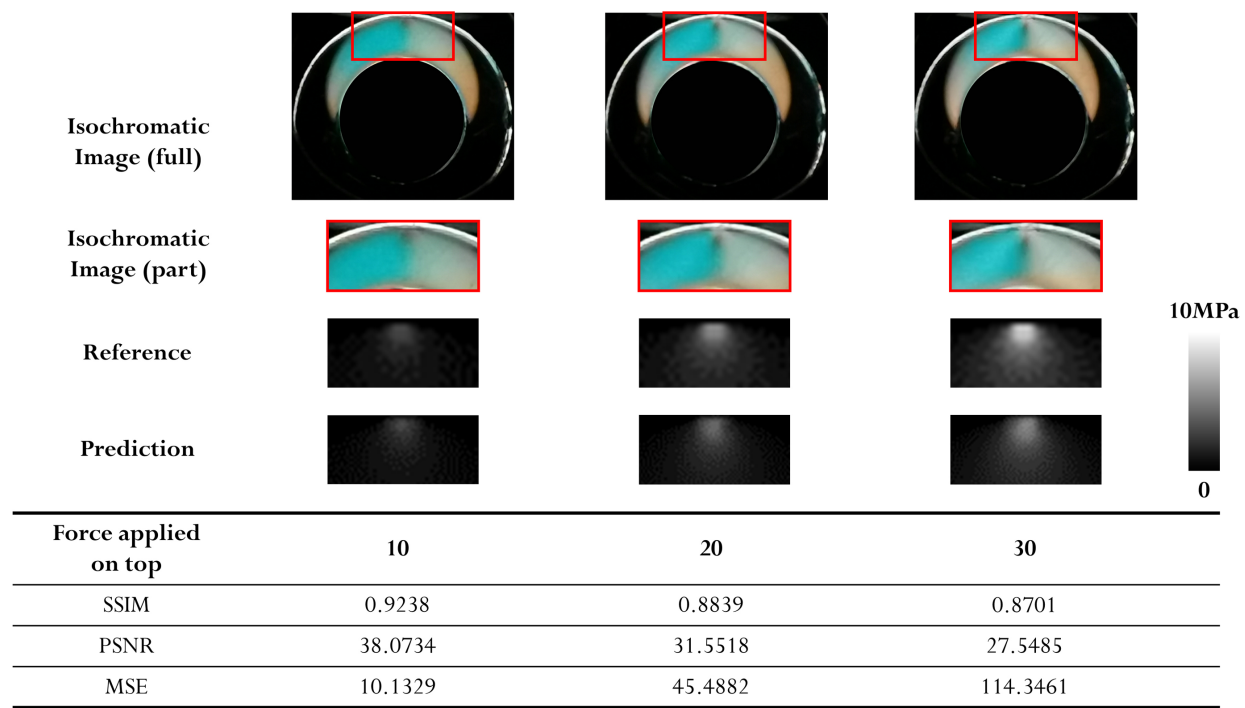


Fig. 8. Predicted stress maps of isochromatic images by using StressUnet and evaluation results on SSIM, PSNR, and MSE in experimental cases. The reference was generated by simulation.

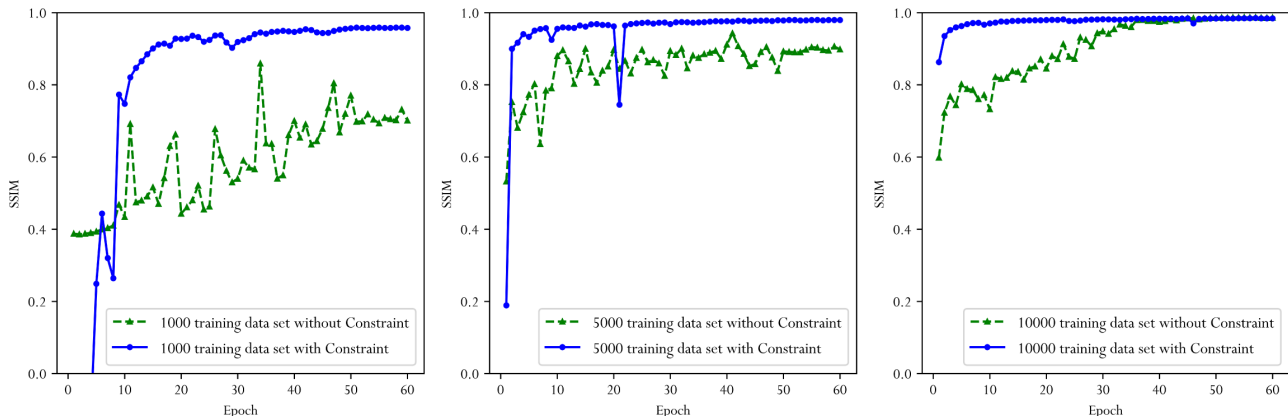


Fig. 9. Performance on validation set when using three groups of training sets. StressUnet with constraint achieved more than 97% SSIM while behaving significantly more robustly than StressUnet without constraint.

Table 3. Ablation Study Performance Comparisons on SSIM, PSNR, and MSE when Using Different Numbers of Training Dataset^a

Training Dataset	Module	SSIM	PSNR	MSE
1000	With constraint	0.9468	30.6144	330.8118
	Without constraint	0.8529	25.3774	691.4577
5000	With constraint	0.9726	33.3868	233.1705
	Without constraint	0.9626	32.9826	270.2348
10,000	With constraint	0.9790	36.0953	199.7511
	Without constraint	0.9789	35.1607	244.7448

^aBold numbers denote the highest scores.

constraint module on all metrics, including a 0.09 boost in SSIM and 20.6% improvement in PSNR. When there were

more images to learn from, two models achieved similar results, but StressUnet with the constraint module still slightly defeated StressUnet without the constraint module.

4. DISCUSSION

Compared with the traditional methods that do not involve deep learning, our model requires only a single image to complete the demodulation, while phase-shifting techniques need at least three images and even more to obtain high-accuracy results. Thus, the configuration to capture isochromatic images is less complicated than that of the phase-shifting technique and carrier fringe method, and has higher robustness, because the polarizer and quarter-wave plate are stationary, which can reduce the mismatch error of the quarter-wave plate. Once our

model has been trained, it can be employed to predict stress distribution. Otherwise, applying the TFP method should update the calibration image to cope with different experiment circumstances. Overall, the universality and generalization of the deep learning model simplify the procedures of data acquisition and data processing.

Instead of simply applying models succeeding in other areas to photoelasticity, we took full consideration of the physical problem. To improve prediction accuracy, we made full use of the spatial fringe information from the input; thus, we chose U-Net architecture for the sake of maintaining global information. In terms of the output, since the stress distribution conformed to the Laplace equation, we contrived a simple and flexible module that rendered powerful representations, and was promising to add in other frameworks to enhance performance. As a result, our model outperformed previous deep-learning-based methods.

Although the stress our model can predict ranges from 0 to 72 MPa due to the composition of the dataset, we are confident that the stress range can be expanded if we add images of higher stress cases into the training set. Moreover, because there is a sharp decrease in training time and number of training sets, it is relatively flexible to adjust the stress range.

5. CONCLUSION

In this work, we proposed StressUnet, a novel convolution neural network based on U-Net that took Resnet as the backbone. Oriented to the stress distribution problem, we added a simple module named constraint, making the stress map consistent with physical law. Compared with previous networks with fully convolutional network (FCN) architecture, we obtained higher predicting accuracy with SSIM over 97%, outperforming the previous method by 5%. We adopted the encoder-decoder structure prevailing nowadays, and used skip connections such as U-Net, inspired by the indispensability of global fringe information in isochromatic images. In regard to the constraint module, its design is simple and flexible but powerful and effective. In contrast to conventional methods, which must take light sources and camera sensors into account, or require a series of images under different polariscope configurations and unwarping algorithms, the end-to-end deep learning network, which needs only a single image, accelerates the stress evaluation and makes instant detection realistic by employing the model on data processing. In spite of the perfect stress prediction on the classic stress model, our framework faced performance degradation in the case of complex patterns and large magnitudes of stress. It provides an opportunity to improve the combination mechanism of global fringe information and local transition. Although the network in this paper specifically resolves the problem of quantifying the stress field by a photoelasticity image, it may contribute to other physical questions and optical applications, such as calculating stress maps through material structures, in which input and output are similar to our task and obey the same physical law.

Funding. Fundamental Research Funds for the Central Universities; National College Students Innovation and Entrepreneurship Training Program.

Acknowledgment. The authors acknowledge the Information Office of Beihang University for supplying high performance computing.

Disclosures. The authors declare no conflicts of interest.

Data availability. Data underlying the results presented in this paper are available in [20], including the isochromatic images and the respective reference stress maps from Figs. 4–7.

REFERENCES

1. K. Ramesh and V. Ramakrishnan, "Digital photoelasticity of glass: a comprehensive review," *Opt. Lasers Eng.* **87**, 59–74 (2016).
2. M. Stoehr, G. Gerlach, T. Hartling, and S. Schoenfelder, "Analysis of photoelastic properties of monocrystalline silicon," *J. Sens. Sens. Syst.* **9**, 209–217 (2020).
3. S. Dix, C. Schuler, and S. Kolling, "Digital full-field photoelasticity of tempered architectural glass: A review," *Opt. Lasers Eng.* **153**, 106998 (2022).
4. Q. Ding, M. Wang, H. Xing, Q. He, L. Ma, and W. Qiu, "Investigation of a fitting phase-shift method for stress analysis using infrared photoelasticity," *Opt. Lasers Eng.* **149**, 106787 (2022).
5. S. Wei, Y. J. Pang, Z. X. Bai, Y. L. Wang, and Z. W. Lu, "Research progress of stress measurement technologies for optical elements," *Int. J. Opt.* **2021**, 5541358 (2021).
6. K. Ramesh and S. Sasikumar, "Digital photoelasticity: recent developments and diverse applications," *Opt. Lasers Eng.* **135**, 106186 (2020).
7. R. Vivek and K. Ramesh, "Residual stress analysis of commercial float glass using digital photoelasticity," *Int. J. Appl. Glass Sci.* **6**, 419–427 (2015).
8. K. Creath, "Phase-shifting speckle interferometry," *Appl. Opt.* **24**, 3053–3058 (1985).
9. S. Sasikumar and K. Ramesh, "Applicability of colour transfer techniques in twelve fringe photoelasticity (TFP)," *Opt. Lasers Eng.* **127**, 105963 (2020).
10. P.-C. Sung, W.-C. Wang, C.-H. Hwang, and G.-T. Lai, "A low-level stress measurement method by integrating white light photoelasticity and spectrometry," *Opt. Laser Technol.* **98**, 33–45 (2018).
11. T. Guo, J. Dong, H. Li, and Y. Gao, "Simple convolutional neural network on image classification," in *IEEE 2nd International Conference on Big Data Analysis (ICBDA)* (IEEE, 2017), pp. 721–724.
12. A. Dhillon and G. K. Verma, "Convolutional neural network: a review of models, methodologies and applications to object detection," *Prog. Artif. Intell.* **9**, 85–112 (2020).
13. V. Badrinarayanan, A. Kendall, and R. Cipolla, "SegNet: a deep convolutional encoder-decoder architecture for image segmentation," *IEEE Trans. Pattern Anal. Mach. Intell.* **39**, 2481–2495 (2017).
14. A. Lucas, M. Iliadis, R. Molina, and A. K. Katsaggelos, "Using deep neural networks for inverse problems in imaging beyond analytical methods," *IEEE Signal Process. Mag.* **35**(1), 20–36 (2018).
15. J. C. Bríñez-de León, M. Rico-García, and A. Restrepo-Martínez, "PhotoelastNet: a deep convolutional neural network for evaluating the stress field by using a single color photoelasticity image," *Appl. Opt.* **61**, D50–D62 (2022).
16. B. Tao, Y. Wang, X. Qian, X. Tong, F. He, W. Yao, B. Chen, and B. Chen, "Photoelastic stress field recovery using deep convolutional neural network," *Front. Bioeng. Biotechnol.* **344**, 818112 (2022).
17. O. Ronneberger, P. Fischer, and T. Brox, "U-net: convolutional networks for biomedical image segmentation," in *International Conference on Medical Image Computing and Computer-Assisted Intervention* (Springer, 2015), 234–241.
18. K. Ramesh, V. Ganeshan, and S. Mullick, "Digital image processing of photoelastic fringes—a new approach," *Exp. Tech.* **15**, 41–46 (1991).
19. K. He, X. Zhang, S. Ren, and J. Sun, "Deep residual learning for image recognition," in *Proceedings of the IEEE Conference on Computer Vision and Pattern Recognition* (2016), pp. 770–778.
20. J. C. Bríñez-de León, M. Rico-García, A. Restrepo-Martínez, and J. W. Branch, "Isochromatic-art: a computational dataset for evaluating the stress distribution of loaded bodies by digital photoelasticity," Mendeley Data, v4 (2020), <https://data.mendeley.com/datasets/z8yhd3sj23/4>.

21. Z. Wang, A. C. Bovik, H. R. Sheikh, and E. P. Simoncelli, "Image quality assessment: from error visibility to structural similarity," *IEEE Trans. Image Process.* **13**, 600–612 (2004).
22. A. Hore and D. Ziou, "Image quality metrics: PSNR vs. SSIM," in *20th International Conference on Pattern Recognition* (IEEE, 2010), pp. 2366–2369.
23. D. P. Kingma and J. Ba, "Adam: a method for stochastic optimization," (2014).
24. A. Paszke, S. Gross, F. Massa, A. Lerer, J. Bradbury, G. Chanan, T. Killeen, Z. Lin, N. Gimelshein, and L. Antiga, "Pytorch: An imperative style, high-performance deep learning library," in *Advances in Neural Information Processing Systems* (2019), Vol. **32**.
25. W. Zhao, "StressUnet," GitHub (2022), <https://github.com/weiliang415/StressUnet>.
26. R. G. R. Prasath, K. Skenes, and S. Danyluk, "Comparison of phase shifting techniques for measuring in-plane residual stress in thin, flat silicon wafers," *J. Electron. Mater.* **42**, 2478–2485 (2013).
27. E. H. Guo, Y. G. Liu, Y. S. Han, D. Arola, and D. S. Zhang, "Full-field stress determination in photoelasticity with phase shifting technique," *Meas. Sci. Technol.* **29**, 045208 (2018).
28. F. Su, B. W. Zhang, and T. H. Li, "High speed stress measurement technique based on photoelastic modulator (PEM) and galvano-scanner," *Opt. Lasers Eng.* **136**, 106306 (2021).
29. C. Lane, D. Rode, and T. Rosgen, "Two-dimensional birefringence measurement technique using a polarization camera," *Appl. Opt.* **60**, 8435–8444 (2021).
30. A. Ajovalasit, G. Petrucci, and M. Scafidi, "Review of RGB photoelasticity," *Opt. Lasers Eng.* **68**, 58–73 (2015).
31. M. Mitsuzuka, Y. Kinbara, M. Fukuhara, M. Nakahara, T. Nakano, J. Takarada, Z. Wang, Y. Mori, M. Kageoka, and T. Tawa, "Relationship between photoelasticity of polyurethane and dielectric anisotropy of diisocyanate, and application of high-photoelasticity polyurethane to tactile sensor for robot hands," *Polymers* **13**, 143 (2020).
32. J. C. B. de León, H. A. Fandiño, A. Restrepo, and J. W. Branch, "Computational analysis of stress map variations by industrial light sources and load additions in digital photoelasticity," *Proc. SPIE* **10751**, 107510G (2018).